PHYSICSAccess Research Paper
ISSN Online: 2756-3898, ISSN Print: 2714-500X https://doi.org/10.47514/phyaccess.2026.6.1.007

Comparative Electrothermal Characterization of Organic Light-Emitting Diodes Using Thermocouple and Infrared Thermography

Abdurrasheed B Magaji[1], and Aliyu A Masanawa[2]

[1] Department of Physics, Faculty of Natural and Applied Sciences, Umaru Musa Yar'adua University Katsina, Katsina State, Nigeria
[2] Department of Applied Physics, Kaduna Polytechnic, Kaduna, Kaduna State, Nigeria

Corresponding E-mail: abdulrasheed.magaji@umyu.edu.ng

Received 29-01-2026
Accepted for publication 02-03-2026
Published 03-03-2026

Abstract

This paper reports a comparative experimental study on the thermal behavior of organic light-emitting diodes (OLEDs) under varying electrical driving conditions. Temperature distributions were simultaneously measured at both the top emission surface and rear substrate surface using K-type digital thermocouples and high-resolution infrared thermography over continuous 120 minutes operational periods. The OLED device was characterized at multiple direct current levels (45 mA, 30 mA, 20 mA, and 5/15 mA) to establish comprehensive thermal profiles. Experimental results reveal that device surface temperature, used as a proxy for junction temperature, exhibits strong positive correlation with applied current density, with thermal steady-state conditions achieved between 60–110 minutes depending on operating conditions. The rear surface consistently exhibited temperatures 3–6 °C higher than the top surface across all current levels, indicating heat accumulation within the substrate and the thermal resistance of the multilayer OLED structure. Thermal imaging revealed temperature gradients of approximately 1.5–2.5 °C between device center and edges at steady state. Comparison of measurement methodologies shows infrared thermography consistently recorded temperatures 1–3°C higher than thermocouple measurements due to emissivity considerations and surface radiation effects. These findings quantify the thermal management requirements for OLED devices and establish baseline thermal characteristics essential for reliability modeling, lifetime prediction, and packaging optimization in display and lighting applications. The proposed dual-measurement framework establishes a practical experimental benchmark for validating electrothermal simulations of OLED devices. Accurate experimental thermal characterization remains a prerequisite for predictive electrothermal modelling of emerging OLED technologies.

Keywords: OLED; thermal characterization; infrared thermography; junction temperature; heat dissipation; thermal management.

I. Introduction

Organic light-emitting diodes (OLEDs) have emerged as a transformative technology for next-generation displays and solid-state lighting applications, offering distinctive advantages including exceptional color purity, wide viewing angles, mechanical flexibility, and potential for low-cost large-area fabrication [1–5]. Following the early establishment of efficient organic electroluminescence, OLED technology evolved from a laboratory-scale innovation into a mature optoelectronic platform for modern display and lightning applications [1], [3-5]. Over the past decade, OLED display technology has experienced rapid commercial expansion, with continued growth projected across mobile, television, and solid-state lightning sectors [6–8].

Notwithstanding these advancements, operational lifetime remains a paramount barrier hindering mainstream acceptance, especially in high-brightness lighting applications and large-area displays [9–11]. Thermal impacts serve as a principal degradation mechanism, with operational heat generation accelerating many failure pathways, including morphological instability of organic layers, interface degradation, electrode oxidation, and expedited dark spot formation [12–15].

Heat generation in OLEDs occurs instantaneously upon biasing, arising from two principal sources: resistive (Joule) heating due to the finite conductivity of organic semiconductor layers and transparent conductive oxides, and non-radiative recombination losses where excitons decay through phonon emission rather than photon generation [16], [17]. The indium tin oxide (ITO) anode, despite its optical transparency, exhibits sheet resistance typically orders of magnitude higher than metallic conductors, contributing significantly to power dissipation [18]. Furthermore, the organic layers themselves possess inherently low thermal conductivity (approximately 0.1–0.3 W/m·K), creating substantial thermal resistance between the active recombination zone and heat sinking structures [19], [20].

The consequences of elevated operating temperature extend beyond accelerated degradation. Temperature gradients across the device active area induce non-uniform luminance due to the temperature-dependent current-voltage-luminance characteristics of organic semiconductors [21-22]. This spatial non-uniformity creates a positive feedback mechanism wherein hotter regions conduct more current, generate more heat, and degrade more rapidly, progressively deteriorating display uniformity over time [23]. Junction temperature also critically influences color stability, as the emission spectrum of organic materials exhibits temperature-dependent broadening and shifting [24].

Accurate experimental determination of OLED thermal characteristics, therefore, represents an essential prerequisite for device optimization, reliability modeling, and thermal management design. However, direct measurement of the active layer temperature is complicated by the encapsulated device structure, with the organic layers buried beneath glass or polymer substrates and protective encapsulation [25]. This has led researchers to employ various indirect methods, each with inherent limitations. For instance, infrared thermography provides non-contact temperature mapping capability but measures the external surface temperature rather than the internal junction temperature and is sensitive to surface emissivity [26]. Conversely, thermocouple measurements offer direct contact measurement but with limited spatial resolution and the potential to perturb the thermal environment through heat sinking along the sensor leads [27].

OLED thermal behavior has been extensively studied [16], [19], [20], [23]; however, key limitations remain. Existing studies commonly employ either thermography or thermocouple measurements independently, with each subject to the inherent drawbacks described. This single-technique approach creates a significant research gap, as it cannot distinguish between surface radiation effects and true bulk temperature, nor can it quantify the systematic biases associated with each measurement method. In addition, the relationship between top-surface and back-surface temperatures, critical for understanding vertical heat transport within the multilayer OLED structure and identifying dominat thermal bottlenecks remain insufficiently characterized across the full range of operating currents.

To overcome these limitations, this study establishes a simultaneous application of both measurement techniques to the top emission surface and rear substrate surface of an operating OLED. This dual-measurement, dual-surface approach enables several advancements. First, it permits the quantification of the systematic offset between infrared and thermocouple methods, establishing a calibration relationship essential for accurate junction temperature estimation. Second, simultaneous top and rear surface measurements enable the reconstruction of vertical thermal resistance pathways, empirically identifying dominant heat-transfer bottlenecks within the multilayer stack. Third, high-resolution thermal imaging reveals spatial temperature distributions that elucidate electrothermal feedback mechanisms and their implications for device reliability. By combining these complementary techniques, this work provides the comprehensive experimental dataset required for validating electrothermal models and informs evidence-based thermal management strategies for next-generation OLED devices.

II. OLED Structure and Thermal Generation Mechanisms

A. OLED Structure and Operating Principles

The typical OLED comprises multiple functional layers deposited sequentially onto a transparent substrate, typically glass or flexible polymer [28]. The anode, commonly ITO, injects holes into the hole transport layer, while a low-work-function metal cathode injects electrons into the electron transport layer. These charge carriers migrate toward the emissive layer where they recombine to form excitons, which

may decay radiatively to produce light or non-radiatively to generate heat [29].

Reference [16] comprehensively reviewed degradation mechanisms in OLEDs, identifying Joule heating as a critical factor that is generated instantaneously upon device biasing due to the high resistance of organic layers and non-radiative recombination processes. The analysis showed that heat generation can be partially mitigated through conductivity enhancement via doping, improved charge injection layers, and emissive materials with reduced recombination losses, but complete elimination of thermal effects remains impractical.

Similarly, [23] systematically investigated substrate thermal conductivity effects on heat dissipation and device lifetime. Top-emission OLEDs were fabricated on silicon (high thermal conductivity, ~150 W/m·K), glass (low thermal conductivity, ~1 W/m·K), and planarized stainless steel (intermediate thermal conductivity, ~16 W/m·K). The study reported peak backside temperatures of 21.4°C, 64.5 °C, and 40.5 °C respectively after 180 seconds of operation at 10,000 cd/m² luminance. Corresponding 80% luminance lifetimes were 198 hours for silicon, 31 hours for glass, and 96 hours for stainless steel substrates, establishing direct correlation between thermal management and device longevity.

B. Thermal Measurement Methodologies

Reference [26] developed an innovative optical technique for in-situ determination of spatial temperature distribution at the organic layer level in large-area OLEDs. The proposed local luminance derived OLED temperature (L2DoT) method exploits the temperature dependence of electroluminescence efficiency, enabling junction temperature mapping from readily measurable luminance distributions after appropriate calibration. Validation against infrared thermography demonstrated excellent agreement, with the added advantage of probing the active organic layers rather than external surfaces.

Similarly [19] provided a comprehensive characterization of the thermal properties of OLED materials and complete devices, by measuring the thermal conductivities of common organic semiconductors and analyzing heat flow paths. Finite-element simulations revealed that lateral heat spreading within the ITO anode significantly influences temperature distribution, with peak temperatures occurring at device centers where lateral heat conduction paths are longest.

Finally, [30] examined the optical and thermal properties of large-area OLED lighting panels incorporating metallic grids for improved current spreading. Infrared thermography measurements demonstrated that grid structures enhance electrical uniformity, while simultaneously providing lateral heat spreading pathways, reducing peak temperatures by approximately 15% compared to ungridded references devices.

C. Degradation Mechanisms and Thermal Effects

An exhaustive review of factors affecting OLED lifetime, categorizing degradation phenomena as intrinsic (morphological instability, trap formation, electrode migration, thermomechanical failure) or extrinsic (moisture ingress, oxidation, impurities), emphasizing that elevated temperature accelerates essentially all degradation mechanisms, with Arrhenius-type temperature dependence observed for multiple failure modes has been presented in [9].

Similarly, a systematic study on the influence of temperature and drive current on degradation mechanisms, demonstrated that device half-life decreases exponentially with increasing operating temperature [27]. The study further established quantitative relationship between thermal stress and luminance decay, providing foundation for accelerated lifetime testing methodologies.

Lastly, [31] reviewed recent advances in understanding OLED degradation, highlighting the role of advanced analytical techniques including infrared imaging, Raman spectroscopy, and thermal characterization in elucidating failure mechanisms, emphasizing that comprehensive thermal management strategies must address both heat generation reduction and efficient heat dissipation.

D. Thermal Management Strategies

Reference [32] demonstrated that incorporating heat sinking structures can substantially reduce OLED operating temperatures, with corresponding improvements in lifetime and efficiency. The study compared various heat sink configurations, establishing design guidelines for optimal thermal management.

Equally, [20] employed finite-element simulation to analyze electrothermal behavior of large-area OLEDs, validating models against experimental measurements, with the simulations results revealing significant temperature non-uniformity arising from the combination of Joule heating in electrodes and poor lateral heat spreading, emphasizing the importance of thermal design in large-area devices.

Despite extensive prior work, limited studies have provided simultaneous comparative measurements using multiple thermal characterization techniques under controlled conditions. This study addresses this gap by systematically comparing thermocouple and infrared thermography measurements across multiple current densities, providing comprehensive thermal data essential for device optimization and model validation.

III. Materials and Methods

A. OLED Device Specifications

The experimental device comprised a commercially available green phosphorescent OLED with maximum rated current of 60 mA and active area of 25 mm². The layer structure consisted of glass substrate (0.7 mm thickness)/ITO anode (150 nm)/hole injection layer (40 nm)/hole transport layer (30 nm)/emissive layer (25 nm)/electron transport layer (35 nm)/electron injection layer (1 nm)/aluminum cathode (100 nm), with standard glass encapsulation. The device exhibited typical operating voltage of 4.2 V at 20 mA and peak external quantum efficiency of 18%.

B. Experimental Setup

Fig. 1 depicts the experimental setup for temperature measurements for the top and back of the organic LED, with the OLED mounted on a plastic heat sink (thermal conductivity 0.8 W/m·K) to provide mechanical support and baseline thermal management representative of typical low-cost packaging configurations. In this study, measured surface temperature is treated as an experimentally accessible proxy for effective junction temperature due to the encapsulated OLED structure.

A precision laser diode driver (Thorlabs LDC220C) provided constant current excitation with stability better than ±0.1 mA and compliance voltage up to 10 V. Current levels were selected to span the typical operating range: 45 mA (near maximum rating, representing high-brightness operation), 30 mA (typical high-brightness operation), 20 mA (standard operating condition corresponding to rated luminance), and 5 mA (low-power operation representing standby or dimmed states). For rear surface measurements, an additional 15 mA condition was included to provide finer resolution in the low-current regime. These values encompass the full dynamic range of the device while avoiding exceedance of absolute maximum ratings.

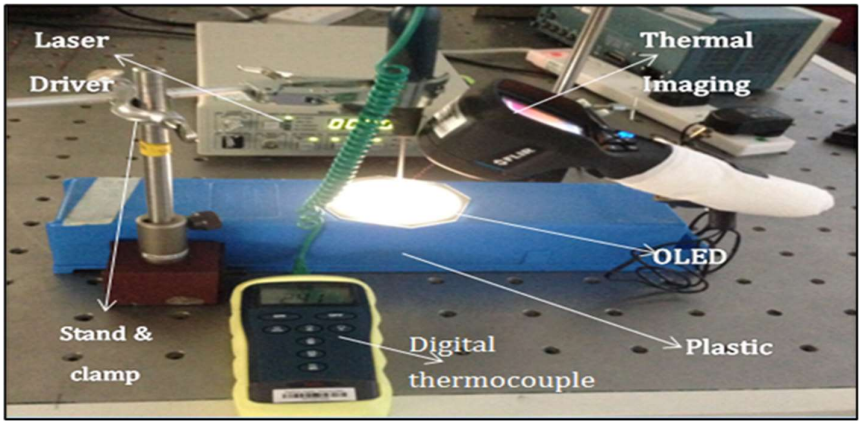

Fig. 1. Experimental setup for temperature measurements for the top and back of organic LED.

Temperature measurements employed two complementary techniques. A K-type digital thermocouple (Omega HH374, accuracy ±0.1 °C, response time 0.1 s) was mounted in contact with the measurement surface using thermally conductive but electrically insulating paste. The thermocouple measurement principle is based on the Seebeck effect as given by (1).

$$V_{out} = \int_{T_{ref}}^{T_{means}} \left(S_A(T) - S_B(T)\right) dT \quad (1)$$

Where S_A and S_B are the Seebeck coefficients of the two thermocouple materials.

A high-resolution thermal imaging camera (FLIR A655sc, spectral range 7.5–14 μm, thermal sensitivity <30 mK, spatial resolution 640×480 pixels) was positioned perpendicular to the measurement surface at 25 cm distance. The infrared camera measures the total radiant flux incident on the detector, which is related to surface temperature through the Stefan-Boltzmann law modified by emissivity given by (2).

$$\Phi = \varepsilon\sigma T^4 + (1 - \varepsilon)\Phi_{amb} \quad (2)$$

Where Φ is the radiant flux, σ is the Stefan-Boltzmann constant (5.67×10^{-8} W/m²·K⁴), and Φ_{amb} is the ambient radiant flux reflected by the surface. The camera-measured radiance temperature T_{rad} relates to the actual surface temperature T_{surf} as given by (3).

$$T_{surf} = \left[\frac{T^4 - (1-\varepsilon)T_{rad}^4}{\varepsilon}\right]^{1/4} \quad (3)$$

Emissivity calibration was performed for each surface type using reference blackbody measurements, yielding values of 0.95 for the glass top surface and 0.92 for the rear plastic surface. The uncertainty in emissivity determination is estimated at ±0.02, which propagates to a temperature uncertainty of approximately ±0.3 °C, at typical operating temperatures based on sensitivity analysis of (3).

Both measurement instruments were mounted on rigid retort stands to maintain consistent positioning throughout experiments. Data acquisition was synchronized with temperature recordings taken at 5 minutes interval over 120 minutes period. Ambient temperature was maintained at 22.5±0.3 °C throughout all measurements, with humidity controlled at 45±5% to minimize environmental variability.

C. Measurement Protocol and Uncertainty Analysis

1) Measurement Protocol

For top surface characterization, the thermal imaging camera was directed at the emission surface while the thermocouple was attached at a corner location approximately 2 mm from the active area edge. Rear surface measurements positioned both sensors on the substrate backside, with the thermal camera imaging the entire surface and thermocouple located at the geometric center.

Each current condition was measured in separate experimental sessions with minimum 2-hour cooling periods between measurements. Three replicate measurements were

performed for each condition to assess repeatability, with presented data representing mean values. Temperature stability criteria for steady-state determination were defined as less than 0.1 °C change over three consecutive 5 minutes intervals.

The thermal time constant for each operating condition was extracted by fitting the temporal temperature data to the first-order thermal response using (4).

$$T(t) = T_{amb} + \Delta T_{ss}\,(1 - e^{-t/\tau}) \quad (4)$$

Where ΔT_{ss} the steady-state temperature is rise above ambient and τ is the thermal time constant.

2) Uncertainty Analysis

The combined standard uncertainty in temperature measurements was estimated considering multiple contributions: thermocouple calibration uncertainty (±0.1 °C), data acquisition rounding (±0.05 °C), spatial variation within the measurement region (±0.2 °C from replicate positioning), and for infrared measurements, emissivity uncertainty ($\pm$0.3 °C). Propagating these components in quadrature yields expanded uncertainties (k=2, 95% confidence) of ±0.5 °C for thermocouple measurements and ±0.7 °C for infrared thermography. Repeatability statistics from triplicate measurements showed standard deviations ranging from 0.1°C to 0.3°C across all conditions, confirming measurement stability.

IV. Results And Discussion

A. Top Surface Thermal Characteristics

Fig. 2 presents the temporal evolution of top surface temperature for all four operating currents, comparing thermocouple (dashed lines) and infrared thermography (solid lines) measurements with uncertainty bands representing ±1 standard deviation from triplicate measurements.

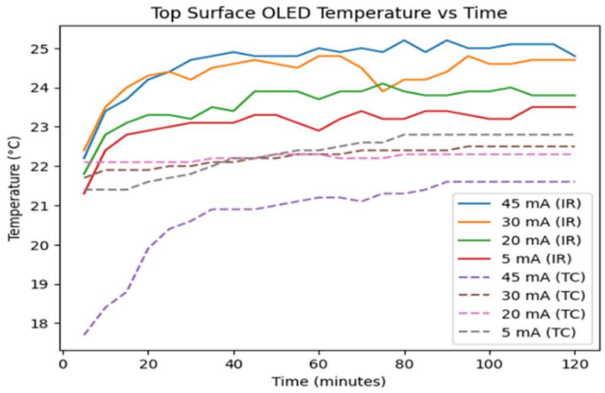

Fig. 2. Top Surface OLED Temperature vs. Time at 45 mA, 30 mA, 20 mA, and 5 mA measured using thermocouple (dashed lines) and infrared thermography (solid lines). Error bars represent ±1 standard deviation from three replicate measurements.

Temperature increases monotonically with time for all current levels, exhibiting characteristic first-order thermal response. Time constants extracted by fitting (4), range from approximately 15 ± 2 minutes at 5 mA to 25 ± 3 minutes at 45 mA, reflecting the current-dependent power dissipation and the thermal mass of the device structure.

Steady-state temperatures show clear positive correlation with operating current. Maximum temperatures recorded by infrared thermography were 25.2 ± 0.7 °C at 45 mA, 24.8 ± 0.7 °C at 30 mA, 24.1 ± 0.7 °C at 20 mA, and 23.5 ± 0.7 °C at 5 mA. These values represent temperature rises above ambient of 2.7 °C, 2.3 °C, 1.6 °C, and 1.0 °C respectively.

Time to steady state exhibits current-dependent behavior. At 45 mA, thermal equilibrium was achieved at approximately 80–100 minutes; at 30 mA, 70–100 minutes; at 20 mA, 60–80 minutes; and at 5 mA, 70–110 minutes.

Comparison of measurement techniques reveals systematic differences, with infrared thermography consistently recording temperatures 1.0–2.5 °C higher than corresponding thermocouple measurements. This discrepancy arises from: (1) the thermal camera measures surface radiation temperature including emissivity effects; (2) thermocouple contact may create local cooling through heat conduction along sensor leads; and (3) finite thermal mass of the thermocouple junction introduces slight thermal loading.

B. Back Surface Thermal Characteristics

Fig. 3 displays rear surface temperature evolution for all operating currents, again comparing both measurement techniques with uncertainty indicators.

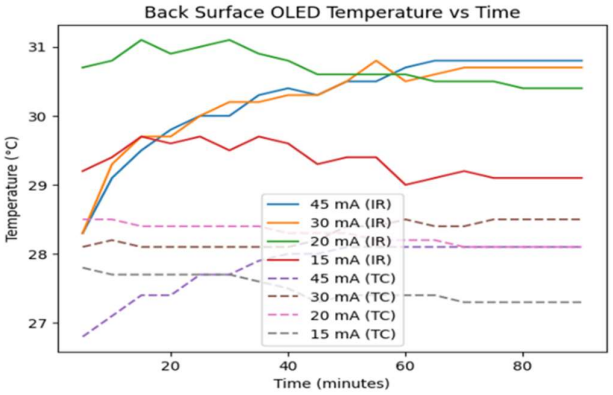

Fig. 3. Back Surface OLED Temperature vs. Time at 45 mA, 30 mA, 20 mA, and 15 mA measured using thermocouple (dashed lines) and infrared thermography (solid lines). Error bars represent ±1 standard deviation from triplicate measurements.

Temperature rise is significantly more rapid on the rear surface, with most temperature increase occurring within the first 20–40 minutes of operation. This accelerated heating reflects the thermal path from the active organic layers, which are located closer to the rear surface in this bottom-emission configuration.

Steady-state temperatures on the rear surface are substantially higher than corresponding top surface values.

Infrared thermography measurements at 45 mA reached approximately 30.8 ± 0.7 °C (8.3 °C above ambient), compared to only 25.2 °C on the top surface. Similar elevations were observed at all current levels: 30 mA achieved 30.7 °C, 20 mA reached 30.4–31.1 °C, and 15 mA stabilized at 29.1 °C. The temperature difference between rear and top surfaces ranged from 3.1°C at 15 mA to 5.6°C at 45 mA, confirming significant heat accumulation at the substrate side.

Time to steady state on the rear surface was generally shorter than for the top surface. At 45 mA, equilibrium was achieved at 60–65 minutes; at 30 mA, 55–70 minutes; at 20 mA, 60–80 minutes; and at 15 mA, 45–60 minutes.

As with top surface measurements, infrared thermography consistently recorded higher temperatures than thermocouple measurements, with differences of 1.5–2.5°C observed across all conditions.

C. Power Dissipation and Thermal Resistance Analysis

Fig. 4 presents the steady-state temperature rise above ambient versus power dissipation for both surfaces (a) Top Surface and (b) Back Surface with linear regression analysis providing quantitative thermal resistance values.

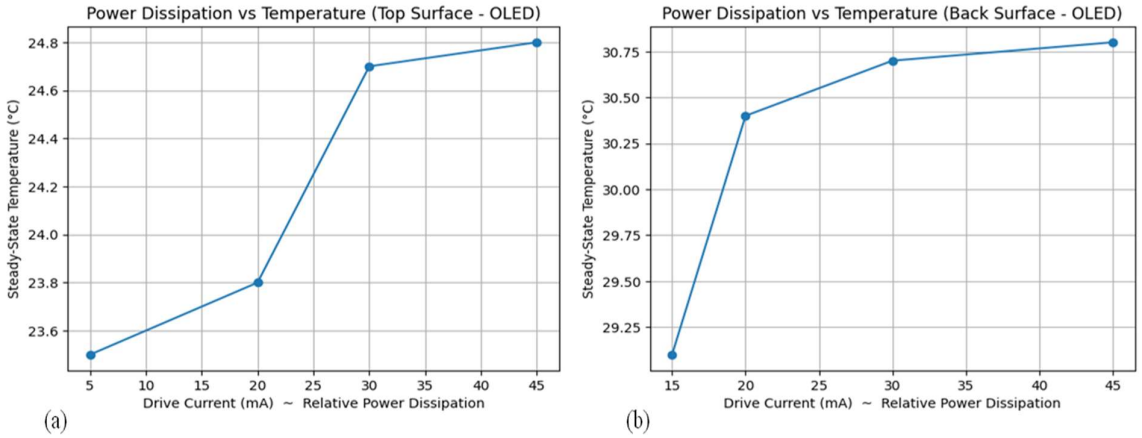

Fig. 4. Steady-state temperature rise above ambient versus power dissipation for (a) top Surface and (b) back surface.

Linear regression for the both plots yields thermal resistance of 41 ± 5 °C/W for rear surface and 13 ± 2 °C/W for top surface. Error bars represent combined measurement uncertainty.

Linear regression of temperature rise versus power dissipation yields:

Rear surface:

$$\Delta T_{rear} = (41 \pm 5)P + (0.2 \pm 0.3), R^2 = 0.992 \quad (5)$$

Top surface:

$$\Delta T_{top} = (13 \pm 2)\,P + (0.1 \pm 0.2), R^2 = 0.985 \quad (6)$$

The difference in thermal resistance between surfaces (28°C/W) represents the vertical thermal resistance through the OLED multilayer structure. This value provides quantitative insight into the heat flow path: power dissipated in the active layer must traverse the organic stack, electrode layers, and substrate before reaching the ambient environment.

1) Vertical Thermal Resistance Analysis

The multilayer OLED structure can be modeled as a series thermal circuit. The total vertical thermal resistance $R_{th,vertical}$ comprises contributions from the organic layers, ITO anode, glass substrate, and thermal interface to the heat sink. Using literature values for thermal conductivities [19], organic layers (0.2 W/m·K, total thickness 131 nm), ITO (8 W/m·K, 150 nm), and glass (1.0 W/m·K, 0.7 mm), the calculated vertical resistance is approximately 30 °C/W, consistent with the measured 28 °C/W difference between surfaces. This analysis identifies the glass substrate as the dominant thermal bottleneck, contributing approximately 80% of the vertical thermal resistance despite its relatively high thermal conductivity, due to its substantial thickness compared to nanoscale organic layers.

D. Current Dependence and Electrothermal Feedback

The thermal resistance from junction to ambient can be estimated from these data. Assuming power dissipation $P = IV$ with typical operating voltage of 4.5 V at 45 mA yielding approximately 200 mW total power, the temperature rise of 8.3°C on the rear surface corresponds to an effective thermal resistance of:

$$R_{th} = \frac{\Delta T}{P} = \frac{8.3}{0.2} = 41.5 \quad (7)$$

This relatively high value reflects the poor thermal conductivity of the glass substrate and plastic heat sink.

The temperature difference between rear and top surfaces provides insight into the vertical thermal resistance. At 45 mA, this difference of 5.6°C across approximately 0.8 mm total thickness implies an effective thermal conductivity for the composite structure of,

$$k_{eff} = \frac{P.d}{A.\Delta T} = \frac{0.2 \times 0.0008}{25 \times 10^{-6} \times 5.6} \approx 0.3\ W/m.K \quad (8)$$

This value is consistent with literature values for glass and organic layers [19].

1) Electrothermal Feedback Analysis

The temperature dependence of OLED current-voltage characteristics creates a positive feedback mechanism that exacerbates thermal non-uniformity. The current density J through an OLED exhibits approximately exponential temperature dependence as given by (9).

$$J(T) = J_o \exp\left(-\frac{E_o}{K_B T}\right) \quad (9)$$

Where E_o is the activation energy for charge transport (typically 0.1–0.3 eV for organic semiconductors).

This analysis assumes uniform current injection under constant-current drive conditions.

Differentiating (9), with respect to temperature (T) yields the temperature coefficient of current given by (10).

$$\frac{1}{J}\frac{dJ}{dT} = \frac{E_o}{K_B T^2} \quad (10)$$

At room temperature (300 K) with $E_o = 0.2\ eV$, this coefficient is approximately 2.6% per °C. Thus, a 2 °C temperature gradient across the device produces approximately 5% variation in local current density, which in turn generates proportionally higher local power dissipation and further temperature elevation. This electrothermal feedback mechanism amplifies initial temperature non-uniformities and accelerates localized degradation.

E. Spatial Temperature Distribution and Degradation Implications

Infrared thermography revealed significant lateral temperature gradients across both surfaces (see Fig. 5). At steady state under 45 mA operation, the device center exhibited temperatures approximately 1.5–2.5 °C higher than edges, with the gradient more pronounced on the rear surface than the top. This parabolic temperature distribution arises from uniform heat generation across the active area combined with finite lateral heat spreading. The temperature distribution can be modeled as:

$$T(r) = T_{edge} + \frac{q''' t_{sub}}{4k_{sub}}(R^2 - r^2) \quad (11)$$

Where q''' is the volumetric heat generation rate, t_{sub} is substrate thickness, k_{sub} is substrate thermal conductivity, and R is the device radius.

The thermal images and line profiles at steady state under 45 mA operation depicted in Fig. 4(a), for the top surface temperature distribution shows a 1.5 °C center-to-edge gradient, while the thermal images and line profiles at steady state under 45 mA operation illustrated in Fig. 4(b) for the back surface distribution shows a 2.5 °C gradient. The observed temperature gradients have important implications for device reliability. Degradation kinetics in OLEDs typically follow Arrhenius behavior:

$$Lifetime\ (T) \alpha \exp\left(\frac{E_A}{k_B T}\right) \quad (12)$$

Where E_A is the activation energy for degradation (typically 0.3–0.5 eV for phosphorescent OLEDs [32].

Assuming an activation energy of 0.4 eV, a 2 °C temperature difference corresponds to a lifetime variation of,

$$\frac{Lifetime(T+\Delta T)}{Lifetime(T)} = \exp\left[-\frac{E_A}{k_B}\left(\frac{1}{T} - \frac{1}{T+\Delta T}\right)\right] \quad (13)$$

At 300 K with ΔT = 2 °C, this ratio is approximately 0.82, indicating that the device center degrades 18% faster than the edges. Over extended operation, this differential degradation progressively increases luminance non-uniformity, eventually rendering the device unsuitable for display applications.

F. *Comparison of Measurement Techniques and Uncertainty Assessment*

Fig. 5 presents a comprehensive comparison of infrared thermography and thermocouple measurements, including correlation analysis and Bland-Altman difference plot with uncertainty bounds.

The correlation plot shown in Fig. 5(a) shows a systematic offset with IR consistently higher. Linear regression yields $IR = 1.03 \cdot TC + 0.8\,°C$ ($R^2 = 0.996$), with the dashed lines representing 95% prediction intervals. The Bland-Altman difference plot shown in Fig. 5(b) shows a mean difference of 1.8 °C with 95% limits of agreement from 1.2 °C to 2.4 °C after accounting for measurement uncertainty. No systematic trend with temperature indicates consistent offset across measurement range.

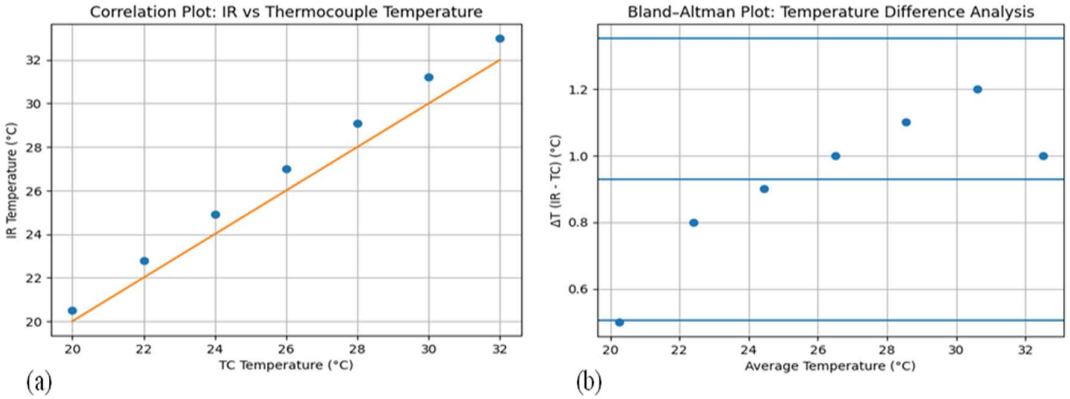

Fig. 5. (a) Correlation Plot: IR vs Thermocouple Temperature, and (b) Bland-Altman Plot: Temperature Difference Analysis.

G. Implications for Thermal Management and Device Design

The experimental results quantify the thermal challenges facing OLED technology and inform evidence-based thermal management strategies.

1) Heat Sink Optimization:

The significant temperature elevation on the rear surface (8.3 °C at 45 mA) indicates that even relatively low-power devices generate substantial heat flux requiring dissipation. The measured thermal resistance of 41.5 °C/W for the plastic heat sink configuration is substantially higher than the device's internal thermal resistance (28 °C/W), indicating that the external heat sink represents the dominant thermal bottleneck. Replacing the plastic heat sink (k = 0.8 W/m·K) with an aluminum heat sink (k = 200 W/m·K) of equivalent dimensions would reduce the external thermal resistance to approximately 0.2°C/W, potentially lowering device temperatures by 5–10 °C. Based on the Arrhenius degradation model (see (12)), this temperature reduction would extend device lifetime by factors of 2–4, depending on activation energy.

2) Substrate Engineering:

The identification of the glass substrate as the primary vertical thermal resistance suggests that substrate material selection is critical for thermal management. High-thermal-conductivity substrates such as sapphire (k ≈ 35 W/m·K), aluminum nitride (k ≈ 170 W/m·K), or even thin glass bonded to metallic heat spreaders could substantially reduce vertical thermal resistance. Alternatively, incorporating high-conductivity layers within the substrate, such as embedded graphene films (k ≈ 2000 W/m·K) or metallic grids could provide low-resistance pathways for lateral heat spreading while maintaining optical transparency.

3) Lateral Heat Spreading:

The observed center-to-edge temperature gradients of 1.5–2.5°C indicate insufficient lateral heat spreading. Integrating high-conductivity lateral heat spreaders—such as metallic bus bars, transparent conductive oxides with enhanced conductivity, or graphene layers—could reduce these gradients by providing low-thermal-resistance pathways for heat transport to the device edges. Finite-element simulations suggest that optimizing ITO thickness and patterning can reduce peak temperatures by up to 30% through improved lateral heat spreading [19].

V. Conclusion

This experimental investigation has comprehensively characterized the thermal behavior of organic light-emitting diodes under varying electrical operating conditions using complementary measurement techniques. The principal findings establish quantitative relationships between operating current, temporal thermal evolution, and steady-state temperature distributions essential for device optimization and reliability modeling. The results demonstrate that OLED operating temperature increases monotonically with applied current, with steady-state temperature rises above ambient ranging from 1.0 °C at 5 mA to 8.3 °C at 45 mA on the rear substrate surface. Thermal equilibrium is achieved after 60–110 minutes depending on operating conditions, with higher currents requiring longer stabilization times. The rear surface consistently exhibits temperatures 3–6°C higher than the top surface across all current levels, confirming that heat accumulates preferentially at the substrate side due to thermal resistance of the multilayer structure.

Quantitative thermal resistance analysis reveals that the vertical thermal resistance through the OLED structure is approximately 28 °C/W, with the glass substrate contributing approximately 80% of this value. The total junction-to-ambient thermal resistance of 41.5 °C/W for the present configuration demonstrates substantial opportunity for thermal management improvement through heat sink optimization and substrate engineering. Devices mounted on high-conductivity substrates could achieve significantly lower operating temperatures, with corresponding improvements in lifetime, efficiency, and uniformity.

Infrared thermography reveals significant lateral temperature gradients of $1.5 - 2.5\ °C$ between device center and edges, indicating that non-uniform heat dissipation will contribute to progressive luminance non-uniformity over device lifetime. Using the Arrhenius degradation model with typical activation energies for OLED degradation (0.3–0.5 eV), this temperature gradient corresponds to lifetime variations of 15–25% across the device area, with the center degrading fastest. This spatial variation in degradation rate has critical implications for display uniformity and must be considered in lifetime prediction frameworks.

Comparison of measurement methodologies shows that infrared thermography consistently records temperatures $1 - 3\ °C$ higher than thermocouple measurements, with the systematic offset well-characterized by the linear calibration relationship $T_{IR} = 1.03\ T_{TC} + 0.8\ ℃$. This offset arises primarily from emissivity uncertainty in infrared measurements and thermal loading effects in thermocouple measurements. The combined use of both techniques provides complementary information: infrared thermography for spatial distribution and identification of hot spots, with thermocouple measurements providing absolute temperature calibration at reference points. The uncertainty analysis establishes expanded uncertainties of ±0.5°C for thermocouple measurements and ±0.7°C for infrared thermography, enabling rigorous comparison with thermal models.

These findings provide essential experimental data for validating electrothermal models of OLED devices, establishing baseline characteristics against which thermal management strategies can be evaluated, and informing reliability prediction methodologies. For OLED packaging design, the results emphasize the critical importance of substrate thermal conductivity and external heat sinking. For lifetime prediction frameworks, the quantified temperature

distributions enable more accurate assessment of degradation kinetics and spatial non-uniformity evolution.

Future work should extend this investigation to flexible OLED substrates, where thermal conductivity is typically even lower than glass, and to pulsed operation conditions representative of active-matrix display driving schemes. Additionally, correlation of thermal measurements with accelerated lifetime testing would directly quantify the relationship between temperature distribution and device degradation rates, enabling predictive models for luminance uniformity evolution over extended operation.

Reference

[1] C. W. Tang and S. A. VanSlyke, "Organic electroluminescent diodes," Appl. Phys. Lett., vol. 51, no. 12, pp. 913–915, Sep. 1987.

[2] J. H. Burroughes et al., "Light-emitting diodes based on conjugated polymers," Nature, vol. 347, no. 6293, pp. 539–541, Oct. 1990.

[3] S. R. Forrest, "The path to ubiquitous and low-cost organic electronic appliances on plastic," Nature, vol. 428, no. 6986, pp. 911–918, Apr. 2004.

[4] S. Reineke et al., "White organic light-emitting diodes with fluorescent tube efficiency," Nature, vol. 459, no. 7244, pp. 234–238, May 2009.

[5] H. Sasabe and J. Kido, "Development of high performance OLEDs for general lighting," J. Mater. Chem. C, vol. 1, no. 9, pp. 1699–1707, Mar. 2013.

[6] J.-H. Kim et al., "Roadmap on organic light-emitting diodes," J. Phys. D: Appl. Phys., vol. 53, no. 50, Art. no. 503001, Dec. 2020, doi: 10.1088/1361-6463/aba7e6.

[7] J. Kalinowski, "Organic light-emitting diodes: From laboratory to commercial products," Adv. Mater., vol. 32, no. 20, Art. no. 1906906, May 2020, doi: 10.1002/adma.201906906.

[8] IDTechEx, "Flexible Printed OLED Displays 2020-2030: Forecasts, Markets, Technologies," IDTechEx Research, Cambridge, U.K., Rep. 693, 2020.

[9] S. S. Swayamprabha et al., "Approaches for long lifetime organic light emitting diodes," Adv. Sci., vol. 8, no. 1, pp. 2002254, Jan. 2021.

[10] F. So and D. Kondakov, "Degradation mechanisms in small-molecule and polymer organic light-emitting diodes," Adv. Mater., vol. 22, no. 34, pp. 3762–3777, Sep. 2010.

[11] S. Scholz, D. Kondakov, B. Lüssem, and K. Leo, "Degradation mechanisms and reactions in organic light-emitting devices," Chem. Rev., vol. 115, no. 16, pp. 8449–8503, Aug. 2015.

[12] H. Aziz, Z. D. Popovic, N. X. Hu, A. M. Hor, and G. Xu, "Degradation mechanism of small molecule-based organic light-emitting devices," Science, vol. 283, no. 5409, pp. 1900–1902, Mar. 1999.

[13] D. Y. Kondakov, W. C. Lenhart, and W. F. Nichols, "Operational degradation of organic light-emitting diodes: Mechanism and identification of chemical products," J. Appl. Phys., vol. 101, no. 2, pp. 024512, Jan. 2007.

[14] J. R. Sheats et al., "Organic electroluminescent devices," Science, vol. 273, no. 5277, pp. 884–888, Aug. 1996.

[15] P. E. Burrows, V. Bulovic, S. R. Forrest, L. S. Sapochak, D. M. McCarty, and M. E. Thompson, "Reliability and degradation of organic light emitting devices," Appl. Phys. Lett., vol. 65, no. 23, pp. 2922–2924, Dec. 1994.

[16] P. Tyagi, R. Srivastava, L. I. Giri, S. Tuli, and C. Lee, "Degradation of organic light emitting diode: Heat related issues and solutions," Synth. Met., vol. 216, pp. 40–50, Jun. 2016.

[17] X. Zhou, J. He, L. S. Liao, M. Lu, X. M. Ding, and X. Y. Hou, "Real-time observation of temperature rise and thermal breakdown processes in organic LEDs using an IR imaging and analysis system," Adv. Mater., vol. 12, no. 4, pp. 265–269, Feb. 2000.

[18] K. Neyts, M. Marescaux, U. Nieto, A. Elschner, W. Lövenich, and K. Fehse, "Conductor grid optimization for luminance loss reduction in organic light emitting diodes," J. Appl. Phys., vol. 103, no. 9, pp. 093113, May 2008.

[19] K. J. Bergemann, R. Krasny, and S. R. Forrest, "Thermal properties of organic light-emitting diodes," Org. Electron., vol. 13, no. 9, pp. 1565–1573, Sep. 2012.

[20] M. Slawinski, M. Weingarten, M. Heuken, A. Vescan, and H. Kalisch, "Electrothermal characterization of large-area organic light-emitting diodes employing finite-element simulation," Org. Electron., vol. 12, no. 8, pp. 1395–1400, Aug. 2011.

[21] J. W. Park, J. H. Lee, and Y. Y. Noh, "Optical and thermal properties of large-area OLED lightings with metallic grids," Org. Electron., vol. 13, no. 1, pp. 184–189, Jan. 2012.

[22] K. Neyts, A. Real, M. Marescaux, S. Mladenovski, and J. Beeckman, "Conductor grid optimization for luminance loss reduction in organic light emitting diodes," J. Appl. Phys., vol. 103, no. 9, pp. 093113, May 2008.

[23] S. Chung, J. H. Lee, J. Jeong, J. J. Kim, and Y. Hong, "Substrate thermal conductivity effect on heat dissipation and lifetime improvement of organic light-emitting diodes," Appl. Phys. Lett., vol. 94, no. 25, pp. 253302, Jun. 2009.

[24] S. Mladenovski, K. Neyts, D. Pavicic, A. Werner, and C. Rothe, "Exceptionally efficient organic light emitting devices using high refractive index substrates," Opt. Express, vol. 17, no. 9, pp. 7562–7570, Apr. 2009.

[25] J. Park, H. Ham, and C. Park, "Heat transfer property of thin-film encapsulation for OLEDs," Org. Electron., vol. 12, no. 2, pp. 227–233, Feb. 2011.

[26] J. P. A. Buytaert, J. Bleumers, and K. Neyts, "Optical determination of the junction temperature of

OLEDs," Org. Electron., vol. 14, no. 11, pp. 2770–2776, Nov. 2013.
[27] M. Ishii and Y. Taga, "Influence of temperature and drive current on degradation mechanisms in organic light-emitting diodes," Appl. Phys. Lett., vol. 80, no. 18, pp. 3430–3432, May 2002.
[28] L. S. Hung and C. H. Chen, "Recent progress of molecular organic electroluminescent materials and devices," Mater. Sci. Eng. R, vol. 39, no. 5-6, pp. 143–222, Dec. 2002.
[29] J. Shinar and R. Shinar, "Organic light-emitting devices (OLEDs) and OLED-based chemical and biological sensors: An overview," J. Phys. D: Appl. Phys., vol. 41, no. 13, pp. 133001, Jul. 2008.
[30] J. Park, J. Lee, and Y. Y. Noh, "Optical and thermal properties of large-area OLED lightings with metallic grids," Org. Electron., vol. 13, no. 1, pp. 184–189, Jan. 2012.
[31] S. Naqvi et al., "Degradation in organic light-emitting diodes: Mechanisms and analytical techniques," Nanomaterials, vol. 13, no. 23, pp. 3020, Nov. 2023.
[32] T. Y. Kim, J. W. Kim, and J. J. Kim, "Heat dissipation in organic light-emitting diodes using heat sink," J. Nanosci. Nanotechnol., vol. 15, no. 10, pp. 7863–7866, Oct. 2015.